Appl Phys B (2010) 101: 263–271
DOI 10.1007/s00340-010-4034-6

Applied Physics B
Lasers and Optics

Hybrid photonic surface-plasmon-polariton ring resonators for sensing applications

M. Chamanzar · M. Soltani · B. Momeni ·
S. Yegnanarayanan · A. Adibi

Received: 17 January 2010 / Revised version: 7 April 2010 / Published online: 8 May 2010

Abstract We introduce a hybrid photonic surface plasmon ring resonator which consists of a silicon nitride (Si_3N_4) dielectric traveling-wave ring resonator vertically coupled to a thin layer of metallic strip ring resonator made of Silver (Ag) on top. The cladding is assumed to be porous alumina on top of the metal layer, which provides more surface area for the adsorption of target molecules and their efficient interaction with the surface plasmon wave excited at the metal-cladding interface. Simulations show that this hybrid structure has a large refractive index sensitivity due to the excitation of surface plasmon waves and also a relatively narrow resonance linewidth due to the large quality factor of the photonic ring resonator. The Finite Element method is used to systematically design the hybrid structure and to investigate the performance of the hybrid resonator as a refractive index sensor. The proposed structure is very compact and can be implemented on a chip in an integrated platform. Thus, it can be used for lab-on-a-chip sensing applications and is capable of being spectrally and spatially multiplexed for muti-analyte sensing.

1 Introduction

Label-free optical sensing is of great recent interest especially in biomedical research for sensing biomolecules or monitoring binding kinetics [1]. In this technique, the target molecules need not be labeled, and their existence is directly sensed typically through the change of refractive index of the interaction medium [1]. This label-free scheme eliminates the tedious preparation process for labeling the molecules and makes the sensing technique fast and simple. Different structures have been used to implement label-free optical sensing, such as surface plasmon resonance (SPR) based sensors [2], photonic waveguide and fiber-based sensors [3, 4], photonic traveling-wave resonator sensors [5, 6], and photonic crystal resonance-based sensors [7]. Each of these techniques is best suited for a particular set of applications. Among all these different methods, SPR-based sensors have been widely used for label-free biomolecule refractive index sensing [2, 8]. Surface plasmon wave is formed through coherent oscillation of free electrons at a metal-dielectric interface. The electromagnetic energy of a surface plasmon mode is highly confined at the metal-dielectric interface. Thus, these modes are very sensitive to the refractive index changes of the dielectric medium. However, conventional SPR sensor systems are usually large and bulky because of the excitation and interrogation mechanism, which is mostly done through prism coupling and angle interrogation [2, 8].

With the increasing need for point-of-care diagnostics, new requirements have emerged for label-free sensors such as compactness, portability, low power consumption, mass production capability, integrability, and multi-analyte detection capability [9–11]. To address these requirements, different techniques have been introduced for the implementation of compact and portable sensors. There have been some efforts to excite SPRs through coupling from a photonic planar waveguide [12] or fiber optics [13]. The waveguide-based SPR sensors can be interrogated through monitoring the transmittance spectrum [12] or through monitoring the coupling spectrum [14]. The fiber-based SPR sensors are formed typically by removing the fiber cladding (by side

---

M. Chamanzar (✉) · M. Soltani · B. Momeni ·
S. Yegnanarayanan · A. Adibi
School of Electrical and Computer Engineering, Georgia Institute of Technology, Atlanta, GA 30332, USA
e-mail: chamanzar@gatech.edu
Fax: +1-404-894-4641

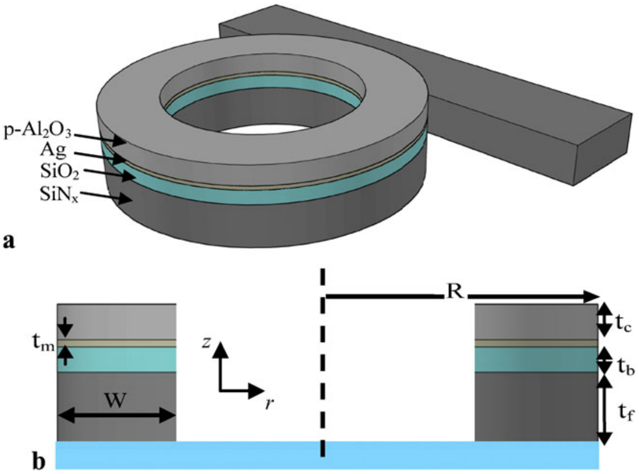

Fig. 1 (**a**) Schematic illustration of the proposed structure consisting of a hybrid plasmonic–photonic ring resonator sensor and a photonic bus waveguide side coupled to the hybrid resonator. The hybrid resonator consists of a photonic traveling-wave resonator with the Si_3N_4 core and a surface plasmon ring resonator made of a thin silver film, separated by a buffer layer of SiO_2. The cladding is a porous layer of alumina as the sensing medium. (**b**) Cross section of the hybrid resonator with the dimensions specified on the figure, R is the radius of the resonator, t_f is the Si_3N_4 film thickness, t_b is the buffer layer thickness, t_m is the metal layer thickness, and t_c is the cladding thickness

polishing the fiber) and depositing a thin metallic layer. This type of structure suffers from cross-polarization interference and different techniques have been introduced to alleviate this problem [13].

It has also been shown that surface plasmon waves can be excited in a metal-semiconductor micropillar cavity [15]. In such a structure, the surface plasmon wave is excited at the metal-semiconductor interface inside the semiconductor where a gain medium is located. This structure is aimed to be used as an on-chip laser. In another work, a silica microresonator covered with a thin metal film is used to excite surface plasmon modes inside the silica microresonator [16]. It has been shown that relatively high quality factor (high-Q) surface plasmon modes can be excited in such microresonators. In both of these structures, the surface plasmon mode is excited inside the microresonator and is not accessible outside the structure for biosensing purposes.

In this paper, we introduce and theoretically investigate a hybrid whispering gallery plasmonic-photonic microring resonator (shown in Fig. 1) for label-free biosensing. The sensor consists of a silicon nitride (Si_3N_4) dielectric traveling-wave ring resonator vertically coupled to a thin layer of metallic strip ring resonator on top covered with a porous alumina (p-Al_2O_3) layer which serves as the sensor interaction medium. In this hybrid resonator, the surface plasmon mode is excited on top of the metallic layer in the porous cladding where the target molecules can efficiently interact with the enhanced electromagnetic field of the surface plasmon wave. The adsorption of target molecules to the interior walls of the porous sensor cladding layer is transcribed into a change in the resonance wavelength of the resonator. One of the unique features of this hybrid resonator sensor is the large sensitivity because of the surface plasmon waves and the relatively high quality factor because of the photonic ring resonator. Moreover, the sensor is very compact and can be implemented into an array format on a planar chip, which is highly desirable for lab-on-a-chip sensing applications.

In practical applications, there is always a need for sensing systems which can detect different analytes at the same time, and there have been ongoing efforts for developing multi-analyte SPR imaging systems [10]. The proposed compact structure in Fig. 1 can be used in a spectrally and/or spatially multiplexed scheme in which many of these hybrid resonators are densely integrated on a chip. Each sensor can have a specific coating associated to a certain analyte. These resonators can be implemented in parallel, each coupled to a separate bus waveguide or they can also be implemented in series, where all of them are coupled to a common bus waveguide. In the case of a spectral multiplexing scheme, on-chip micro-spectrometers [17, 18] can be used to track small shifts in the resonance wavelength.

In this paper, we first discuss the principle of operation and the design procedure for this hybrid resonator in Sect. 2. Subsequently, the performance of this structure is analyzed, and the effect of different device parameters is investigated in Sect. 3. Then in Sect. 4, the possibility of the implementation of the structure in different material platforms, the fabrication procedure, the issue of coupling and possible options for that, and the comparison with other structures are discussed. Concluding remarks are given in Sect. 5.

2 Principle of operation and design of the proposed structure

2.1 Principle of operation

The schematic of the proposed structure is illustrated in Fig. 1(a). It consists of a hybrid plasmonic-photonic traveling-wave ring resonator that is side coupled to a photonic bus waveguide. Figure 1(b) shows the cross section of the hybrid resonator with different dimensions specified. The hybrid resonator is a multilayer traveling-wave ring resonator consisting of a dielectric layer (Si_3N_4) which acts as a dielectric resonator, and a surface plasmon ring resonator (in the form of a thin ring metal strip). The metal strip is assumed to be silver (Ag) here. The surface plasmon resonator and the photonic resonator are separated by a buffer layer which is assumed to be silicon dioxide (SiO_2). The cladding is assumed to be a porous material (alumina (p-Al_2O_3)) which acts as the sensing medium where the target molecules can be adsorbed. The substrate is silicon dioxide. As shown in Fig. 1(b), R is the radius of the resonator, t_f is the Si_3N_4 film thickness, t_b is the buffer layer thickness, t_m is the metal layer thickness, and t_c is the cladding thickness.

The surface plasmon ring resonator mode and the dielectric traveling-wave resonator mode in the structure shown in Fig. 1 are strongly coupled to each other and thereby form a hybrid mode. The photonic bus waveguide shown in Fig. 1(a) is made of a Si_3N_4 ridge on the substrate and carries the optical light wave. This bus waveguide is side coupled to the resonator structure to excite the resonator mode. The transmittance spectrum of the waveguide exhibits a dip at the resonance wavelength of the hybrid structure. When the coupling conditions of the waveguide to the hybrid resonator are optimally engineered (i.e., under critical coupling condition), the coupling is maximized. The excitation of the surface plasmon wave at the interface of the metal and the p-Al_2O_3 cladding results in a large enhancement of electromagnetic fields inside the cladding. When the target molecules are adsorbed to the walls of the pores inside the p-Al_2O_3 layer, the average refractive index of the cladding is changed, and consequently, the resonance wavelength of the resonator shifts. This wavelength shift can be tracked by monitoring the spectral location of the relatively high-Q resonance feature of this resonator at the output of the bus waveguide. The cladding porous layer not only acts as a host for target molecules, but also enhances the performance of the sensor. It has been shown that using a high-index porous cladding layer such as p-Al_2O_3 or p-TiO_2 on top of conventional bulk SPR sensors greatly enhances their response [14, 19, 20]. Like other sensing platforms, different surface coatings can be used on the pore walls of the proposed sensors for target analyte binding; and depending on the surface coating and the target analyte of interest, the sensor can be either reusable or disposable [21].

2.2 Design of the hybrid resonator

The hybrid resonator in Fig. 1 is a traveling-wave resonator. To design such a resonator, we start with the equivalent hybrid ridge waveguide that forms the ring resonator and has the same cross-sectional dimensions as the ring resonator shown in Fig. 1(b) to obtain the effective index of the hybrid guided mode at each wavelength. This hybrid waveguide supports TM-like confined modes (i.e., magnetic field in the plane of the waveguide), which will be the mode type of interest throughout this paper. The effective index of this waveguide mode can then be used as the initial guess to analyze the hybrid ring resonator using a rigorous FEM analysis. The design parameters for the waveguide structure are the dimensions, as illustrated in Fig. 1(b), and the material properties of different layers. In the hybrid sensor introduced in this paper, the substrate is assumed to be SiO_2, with the refractive index of $n = 1.444$. The dielectric resonator is assumed to be Si_3N_4, which has a refractive index of $n = 2$ and enables the operation of the device in the visible range of spectrum. The buffer layer is assumed to be SiO_2, which can be easily deposited on top of Si_3N_4 using plasma enhanced chemical vapor deposition (PECVD). The metal layer is assumed to be Ag that supports surface plasmon modes in the visible range of spectrum. Empirical material properties from [22] are used for the Ag film in our analysis. The cladding layer is chosen to be porous alumina (p-Al_2O_3), which can function as a host for biomolecules. The porosity of this layer can be chosen according to the size and characteristics of the target biomolecules. In our simulations, we have assumed a porous Al_2O_3, with the pore radius of 7.5 nm and pore density of $5 \times 10^{10}\ \text{cm}^{-2}$, which according to Maxwell–Garnett approximation [19, 23] has a refractive index of 1.59.

The thickness of the porous cladding layer (t_c) effectively determines the index of the medium above the metallic layer, which in turn affects the effective index of the surface plasmon mode. It has been shown that $t_c = 200$ nm results in a high sensitivity in a bulk surface plasmon resonance sensor [19]. Therefore, as a practically reasonable value, we set $t_c = 200$ nm. The thickness of the metallic layer is assumed to be $t_m = 50$ nm which is a typical thickness used in many bulk SPR sensors. The width of the structure (w) determines the effective index of the supermode. The thickness of the Si_3N_4 ridge (t_f) together with the width of the structure determines the effective index of the ridge waveguide mode. The buffer layer thickness determines the strength of coupling between the dielectric ridge waveguide mode and the surface-plasmon-polariton mode of the metal-cladding interface. When the buffer layer is very thick, the coupling is very weak and the supermode can be considered as the linear combination of two individual modes of the surface plasmon waveguide and the dielectric waveguide. As the buffer layer thickness is decreased, the two waveguide structures start affecting the modes of each other, and the coupling becomes strong.

Dispersion of the hybrid waveguide structure is calculated using FEM analysis and is plotted in Fig. 2(a) as the real part of effective index of the waveguide structure versus the wavelength for a width of $w = 400$ nm, Si_3N_4 ridge thickness of $t_f = 200$ nm, and a buffer layer thickness of $t_b = 120$ nm. The mode profiles corresponding to the upper and lower branch at a wavelength of $\lambda_0 = 625$ nm are shown in Fig. 2(b) and 2(c), respectively. The two supermodes of this structure shown in Fig. 2 are the result of splitting of the surface plasmon mode and the dielectric waveguide mode that are strongly coupled to each other. It can be seen that the

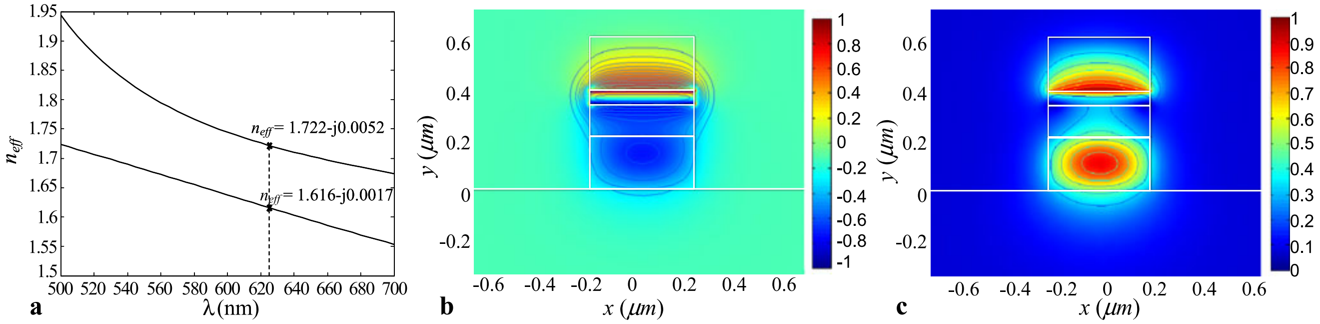

Fig. 2 (**a**) Dispersion of the hybrid waveguide ($w = 400$ nm, $t_f = 200$ nm, $t_m = 50$ nm, $t_b = 120$ nm, $t_c = 200$ nm) calculated using FEM analysis. There are two supermodes at each wavelength. The real part and imaginary part of the effective indices at a wavelength of $\lambda_0 = 625$ nm are indicated on each branch. (**b**) Field profile of the H_x component of the upper branch mode obtained at the wavelength of $\lambda_0 = 625$ nm. (**c**) Field profile of the H_x component of the lower branch mode obtained at the wavelength of $\lambda_0 = 625$ nm

two supermodes have opposite symmetry. It should be noted that as the buffer layer thickness is decreased, the splitting of the modes becomes larger. The lower branch mode (shown in Fig. 2(c)) has a lower effective index and a lower loss, and therefore is of more interest for practical applications. The effective index of the hybrid waveguide for this mode with the aforementioned dimensions and material properties is calculated to be $n_{\mathrm{eff}} = 1.616$–j0.0017 at the operation wavelength of $\lambda_0 = 625$ nm.

Once the effective index of the hybrid ridge waveguide is known, we can insert this effective index as an approximate initial value in the ring resonator dispersion, i.e.,

$$k_0 n_{\mathrm{eff}}(2\pi R_c) = 2m\pi, \qquad (1)$$

to obtain the initial guess for a rigorous FEM simulation of the hybrid traveling-wave ring resonator. In this equation, $k_0 = 2\pi/\lambda_0$ is the free-space wavevector, m is the azimuthal mode order, and n_{eff} is the effective index of the hybrid equivalent ridge waveguide obtained earlier. Finally, $R_c = R - w/2$ is the center radius of the ring resonator. As an example, an azimuthal mode number $m = 114$ gives the resonance wavelength $\lambda_0 = 623.47$ nm for the hybrid ring resonator with a radius of $R = 7.2$ μm. This radius is chosen as a practical value for a compact structure. Note that too small radii result in performance degradation due to the bending loss while too large radii result in large structures.

Having the approximate resonance wavelength (λ_0) and the azimuthal mode number (m), the next step is to use rigorous FEM analysis to obtain the exact modes of the hybrid ring resonator. The axial symmetry of the structure is used to reduce the numerical computation to a two-dimensional analysis at a cross section of the resonator using a FEM code in the cylindrical coordinates [24]. The FEM analysis gives the resonance wavelength of $\lambda_0 = 625.44$ nm for $m = 114$, which is close to the approximated value of $\lambda_0 = 623.47$ nm obtained from (1). The free spectral range of the resonance mode of this structure calculated from FEM simulations is 4.54 nm. It should be noted that the hybrid resonator structure has another (undesired) mode, which corresponds to the higher branch mode of the hybrid waveguide in Fig. 2(b). This mode is not considered in our design as it has considerably higher loss and thus lower quality factor.

The good agreement between the numerical result for the resonant wavelength obtained using rigorous FEM simulation and the result obtained from the effective index modeling using equivalent waveguide analysis suggests that the effective index modeling is a good approximation for the initial guess of FEM analysis and is useful to design and analyze the structure.

The normalized radial field profile (H_r component) for the hybrid resonator structure calculated using FEM simulations is plotted in Fig. 3. Similar to the case of the hybrid waveguide mode depicted in Fig. 2(c), it can be seen from Fig. 3 that the surface plasmon mode and the dielectric guided mode are strongly coupled to each other and form a supermode. The excitation of the surface plasmon polariton at the metal-cladding interface causes the enhancement of the electromagnetic field at the metal-cladding interface where the resonator mode has maximum interaction with the target molecules.

Another interesting feature in Fig. 3 is the fact that the mode is inclined towards the outer radius. In fact, the surface plasmon mode of the metal strip by itself is radiative at this radius without being coupled to a dielectric guiding structure, and the bend radius at which it can support a bound mode is much larger than what we have used here. However, the hybrid structure in which a dielectric resonator and a plasmonic resonator are strongly coupled has the appropriate effective index to support a non-radiative mode.

3 Performance analysis

In order to evaluate the performance of the hybrid resonator designed in the previous section as a refractive index sensor,

Fig. 3 Mode profile of the hybrid ring resonator ($R = 7.2$ μm, $w = 400$ nm, $t_f = 200$ nm, $t_m = 50$ nm, $t_b = 120$ nm, $t_c = 200$ nm) is shown. The normalized radial component of the magnetic field (H_r) is illustrated in this figure

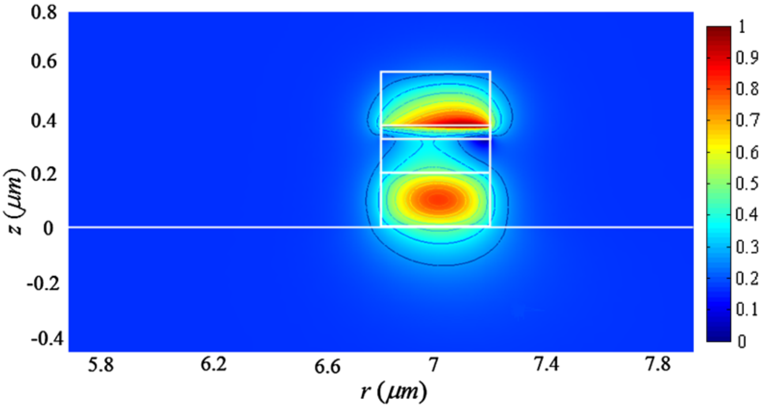

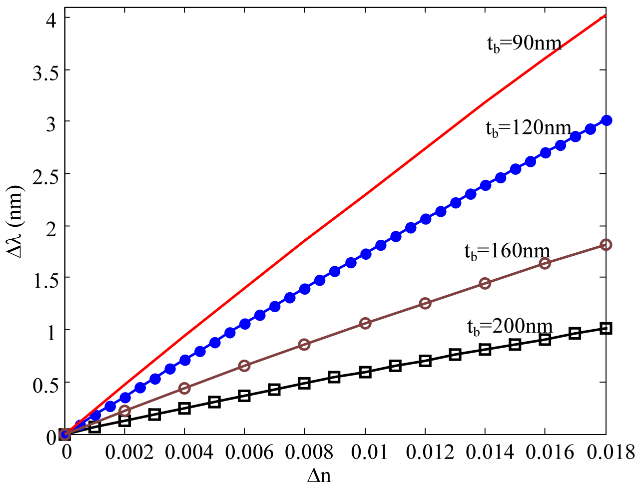

Fig. 4 Spectral shift of the resonance versus refractive index changes of the cladding layer for different buffer layer thicknesses is plotted. All the other parameters are fixed as indicated in the caption of Fig. 3

we have changed the refractive index of the cladding layer and calculated the shift of the resonance wavelength ($\Delta\lambda$) using FEM simulations. The initial refractive index of the p-Al_2O_3 is assumed to be 1.59, and it is increased to 1.608 in small steps of $\Delta n = 10^{-3}$. For the FEM simulations, the domain of the solution is meshed with triangular elements with quartic Lagrange functions [24]. To ensure the convergence of the results, the average size of the elements in the simulation are: 15 nm in the Si_3N_4 layer, 12 nm in the buffer layer, 5 nm in the metal layer, and 6 nm in the cladding. The calculated resonance wavelength shift versus the refractive index change of the cladding for different buffer layer thicknesses (t_b) is plotted in Fig. 4. The slope of each curve in Fig. 4 represents the sensitivity ($S = \Delta\lambda/\Delta n$) of the sensor for the corresponding value of t_b. It can be seen that when the buffer layer thickness is decreased, the sensitivity is increased. In this case, the surface plasmon mode and the guided mode of the dielectric resonator are coupled more strongly, and a stronger field interacts with the molecules. On the other hand, as the buffer layer thickness is increased, the coupling between the two modes becomes weaker and the sensitivity decreases.

The detection limit of the sensor (DL) depends on the sensitivity as well as the resolution of the sensor [25],

$$\mathrm{DL} = \frac{\Re}{S}. \tag{2}$$

The resolution, $\Re$, is proportional to the linewidth of the resonance ($\delta\lambda$), and it inversely depends on the signal-to-noise ratio in the system (which depends on the detection mechanism used). To evaluate the performance of the proposed sensor, the linewidth of the resonance must also be investigated. In the proposed structure, the sources of resonator energy loss that contribute to the broadening of the lineshape are mainly (i) the surface plasmon mode loss originating from the metal material loss, (ii) scattering loss from fabrication imperfections and sidewall roughness, (iii) radiation loss, and (iv) the coupling of the energy to the waveguide. In our calculations, we have considered the effect of surface plasmon mode loss by considering the frequency dependent metal material loss from empirical data of [22]. Also, the effects of scattering loss from the Si_3N_4 ridge sidewalls and the radiation loss are taken into account by assuming an intrinsic quality factor of $Q_s = 20000$ for the dielectric ring resonator. When the radius of the ring resonator is not very small for the radiation loss to dominate, this mostly depends on the quality of fabrication and can be improved. However, since the intrinsic quality factor of the proposed hybrid device is dominated by the metal material loss, there is no stringent requirement on the fabrication quality; and the hybrid device is tolerant to the fabrication imperfections. The overall effect of the metal material loss and the scattering loss can be lumped into an intrinsic quality factor ($Q_0 = (Q_m^{-1} + Q_s^{-1})^{-1}$), where Q_m is the quality factor associated with the metal material loss. The effect of coupling loss originating from the coupling to and from the waveguide is considered by using the coupling Q, i.e., Q_c. The overall quality factor of the hybrid resonator is then the

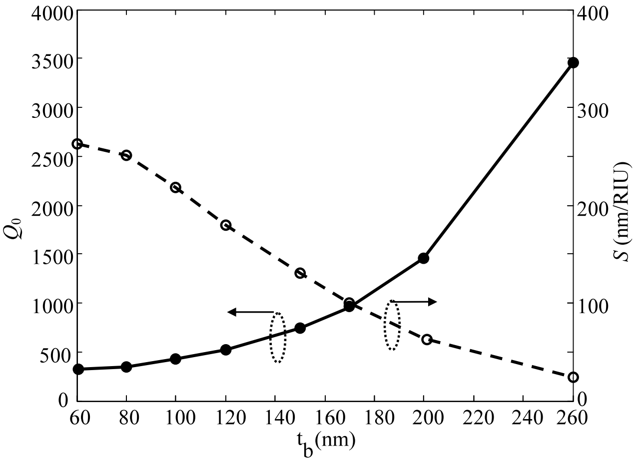

Fig. 5 Intrinsic quality factor (Q_0) of the hybrid resonator ($R = 7.2$ µm, $w = 400$ nm, $t_f = 200$ nm, $t_m = 50$ nm, $t_c = 200$ nm) and the sensitivity (S) versus the buffer layer thickness (t_b)

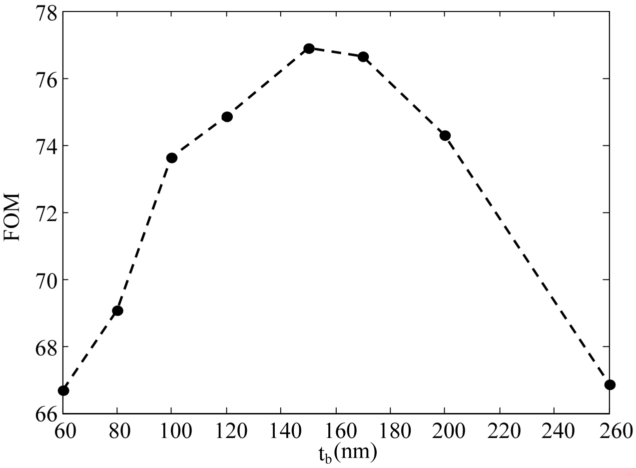

Fig. 6 Figure of merit (FOM) versus buffer layer thickness of the hybrid resonator ($R = 7.2$ µm, $w = 400$ nm, $t_f = 200$ nm, $t_m = 50$ nm, $t_c = 200$ nm)

loaded Q, i.e. $Q_L = (Q_0^{-1} + Q_c^{-1})^{-1}$ which is maximum under critical coupling condition [26] where $Q_c = Q_0$.

The sensitivity (S) and the resonator intrinsic quality factor (Q_0) are plotted in Fig. 5 versus the buffer layer thickness (t_b). It can be seen that as t_b is increased, the sensitivity is decreased because there would be less mode overlap between the surface plasmon mode and the dielectric mode. On the other hand, the resonator intrinsic quality factor (Q_0) increases as t_b is increased because the contribution of metal loss in the overall mode quality factor is decreased. These two effects compete in opposite direction, smaller Q_0 results in wider resonance peaks and more difficulty in detecting a small shift in the center wavelength of resonance, while larger S results in a larger shift in the resonance wavelength for a given index change. Due to this trade-off, there is an optimum value for t_b, which depends on design criteria and the overall desired performance.

To investigate the effect of this trade-off in the design of the proposed sensor quantitatively, we use a figure of merit (FOM) [27], defined as

$$\mathrm{FOM} = \frac{(\Delta\lambda/\Delta n)}{\delta\lambda}, \tag{3}$$

where $\delta\lambda$ is the linewidth of the resonance when the loaded Q, under the critical coupling condition (i.e., $Q_L = Q_0/2$), is considered ($\delta\lambda = \lambda_0/Q_L$). The numerator in (3) is the sensitivity (S) as defined earlier. The detection limit defined in (2) is inversely proportional to FOM, and the proportionality factor depends on the overall signal-to-noise ratio in the detection mechanism [25]. Therefore, FOM is independent of the signal-to-noise ratio and can be used for the assessment of the performance of any resonance-based refractive index sensing structure. FOM as defined in (3) corresponds to a full linewidth shift of the resonance wavelength. The larger the FOM, the better the performance of the device is. One key parameter in the design of the proposed structure is the buffer layer thickness. In order to investigate the effect of this parameter, FOM for the hybrid resonator with the parameters of $R = 7.2$ µm, $w = 400$ nm, $t_f = 200$ nm, $t_m = 50$ nm, $t_c = 200$ nm, is plotted in Fig. 6 versus the buffer layer thickness. The small value of FOM at very small t_b ($t_b < 100$ nm) is due to small values of Q_0 and therefore large values of $\delta\lambda$. On the other hand small values of FOM at large t_b ($t_b > 200$ nm) is due to small values of sensitivity (S).

As is shown in Fig. 6, there is an optimum operation region around $t_b = 150$ nm, where the FOM is maximum. It can be seen in Fig. 6 that the optimum operation point is not very sensitive to the buffer layer thickness around the optimum operation thickness. Therefore, in practice slight changes of the buffer layer thickness during the fabrication of the device does not seriously affect the performance.

As a comparison, FOM is calculated for a fiber-based SPR sensor [13] to be FOM = 71.4, which is comparable with the performance of our proposed sensor. This means that the performance of the proposed structure is on the same order as the other SPR sensing devices; however, this performance is achieved with a much more compact size and in an integrated platform. On the other hand, the values of FOM for different localized surface plasmon resonance (LSPR) nanoparticle sensors are reported to be less than 4 [27], which are much less than the values of FOM in our proposed device (see Fig. 6). This superior performance is of course achieved at the expense of larger sensing volume in our proposed sensor compared with a single plasmonic nanoparticle LSPR sensor. More detailed comparison will be discussed in Sect. 4.3.

4 Discussion

4.1 Different material platforms and fabrication

The hybrid resonator structure in Fig. 1 is proposed in a Si_3N_4 material platform with Ag as the metal material and with alumina as the cladding sensing layer, and it was designed to work in the visible range of spectrum. However, it can be easily implemented using other materials such as silicon in a silicon-on-insulator (SOI) platform for use in infrared range of spectrum. The effective index of the dielectric guided wave resonator mode in Si is larger than that of the same guided wave resonator implemented using Si_3N_4. To satisfy the optimum coupling condition between the dielectric guided wave resonator mode in Si and the surface plasmon mode of metal-cladding interface either a higher index cladding material such as a low porosity alumina, a porous titanium dioxide, or a porous silicon material can be used or the dimensions can be changed.

The choice of metal for the plasmonic layer is not limited to Ag. Other metals such as gold and aluminum can also be used. Gold is used widely in conventional SPR sensors, since it is biocompatible, and unlike silver, it does not oxidize easily. However, it has more loss compared to silver in the visible range of the spectrum. The thickness of the metal layer can be decreased to alleviate this problem.

Using a porous layer in the structure of the proposed hybrid resonator causes the sensitivity of the resonator to increase. In fact, when the target molecules adsorb to the walls of the pores, they form a thin layer, which causes the average refractive index to increase. The porous material provides more surface area for the adsorption of the target molecules and also enhances the interaction of the surface plasmon wave and the target molecules. The pore size provides a means of more specific sensing of the molecules according to their size [19]. Also, special surface coating may be employed on the pore walls to provide more specific sensing mechanism [19]. Other porous materials such as titanium dioxide (TiO_2) or polymer matrices can also be used as the sensing layer.

The fabrication of the device can be carried out by first depositing a thin layer of SiO_2 (buffer layer) on top of a Si_3N_4 film seated on a SiO_2 substrate using plasma enhanced chemical vapor deposition (PECVD) technique. Then, the substrate is covered with a layer of electron-beam resist using spin coating and the ring resonator and bus waveguide can be patterned by using electron-beam lithography (EBL) followed by plasma etching of the Si_3N_4. Then, the entire structure except the ring resonator region is masked in a subsequent EBL lithography step, and the metal layer (e.g., silver in our design) and subsequently aluminum is deposited using electron-beam evaporator followed by a lift off process. In the next step, the aluminum layer is chemically anodized to form a porous Al_2O_3 layer. The alignment of the patterns in the two lithography steps needs special precautions to assure good accuracy. It should be noted that the quality factor of the hybrid resonator is primarily limited by the metal material loss and fabrication imperfections such as the roughness of the sidewalls do not have profound effects on the performance of the device.

4.2 Coupling to the hybrid resonator

In the hybrid resonator system introduced here, the transmittance of the bus waveguide is used as the sensing signal. The structure has the best performance when it works under the critical coupling condition. In the critical coupling regime the power in the waveguide is completely coupled to the resonator and the signal-to-noise ratio is maximized [28]. The overall intrinsic quality factor of the hybrid resonator is determined by the material properties and the dimensions, especially the buffer layer thickness. These parameters are determined by the required performance measures such as the required detection limit and the minimum required linewidth. In some cases, satisfying the critical coupling condition with a straight waveguide side coupled to the resonator might not be trivial due to the small amount of coupling. To address this issue and achieve the critical coupling, we can either use concentric coupling scheme (where the waveguide goes around the resonator) or implement the resonator as a racetrack (where the coupling length can be much longer) [29–31]. For the proposed example in Sect. 2.2, an intrinsic quality factor of $Q = 739.4$ was obtained for a buffer layer thickness of $t_b = 150$ nm (as shown in Fig. 5). By employing the method introduced in [31], it can be shown that the critical coupling condition is achieved by using a concentric coupling scheme in which a 350 nm × 200 nm bus waveguide wraps around the hybrid microring for 60 degrees at a gap distance of 100 nm. This makes the fabrication of the proposed sensors using conventional nanofabrication facilities (e.g., electron-beam lithography and dry etching) easily achievable.

4.3 Comparison with other sensing mechanisms

Different implementations of SPR sensors have been proposed both in bulk form [2, 8] and using guided wave optics such as planar waveguides [12] and fiber optics [13]. Also, localized surface plasmon resonance (LSPR) sensors have been proposed [27]. The SPR-based sensors have shown a promise for fast and effective label-free biosensing and have been used in many biomedical studies [1]. The sensitivity of such SPR sensors is usually very high [2, 13], and the resonance linewidth, mostly determined by the surface plasmon resonance, is large. The performance of the proposed hybrid resonator sensor, according to the figure of merit defined in Sect. 3 ($\text{FOM} = 76.9$), is comparable to the performance of a fiber-based SPR sensor (FOM = 71.4) [13]. However, the proposed structure is much more compact and can be implemented on a chip in an integrated platform which better conforms to the requirements of applications such as point-of-care biosensing. Another important point is that the linewidth of resonance is much smaller for the hybrid resonator compared to conventional bulk or waveguide-based SPR sensors [13]. This makes the spectral multiplexing of the hybrid resonator more viable and many of them can be integrated on a chip to form a spectrally multiplexed array. The performance of the proposed sensor in terms of FOM (FOM = 76.9) is much superior to the performance of LSPR sensors that have FOM values less than 4 [27]. On the other hand, the mode volume of the proposed sensor is much larger than that of individual LSPR nanoparticle sensors. This means that the amount of required analyte for the proposed sensor is larger than that for the LSPR sensors. For the given example in Sect. 2.2, the sensing medium (i.e., the porous alumina layer) has a total volume of 3.5 μm^3, which is about four orders of magnitude larger than the sensing medium surrounding a typical LSPR nanoparticle [27]. However, although the total volume of analyte required to bind to the sensor surface is very small for conventional LSPR sensors, delivering a very small amount of analyte to the sensing sites of LSPR nanoparticles is quite challenging [32]. Moreover, coupling of light to individual LSPR nanoparticles is not very efficient.

As another alternative technology, on-chip dielectric microresonators have been proposed for label-free index sensing [5, 33–35]. For example, a Si_3N_4-based microdisk with a radius of $R = 15$ µm has been proposed with a sensitivity of $S \approx 22.8$ nm/RIU [33]. The figure of merit for this structure can be calculated to be FOM = 142.8. Another example, is a glass-based microring resonator with a radius of $R = 60$ µm which has a sensitivity of $S \approx 141$ nm/RIU [34]. The FOM can be calculated for this structure to be FOM = 1111. It can be seen that these structures have a larger size compared to the proposed hybrid resonator and the sensitivity is smaller than the proposed hybrid resonator, in the former case [33], and comparable with the sensitivity of the proposed structure, in the latter case [34]. However, these resonators have better performance in terms of the FOM due to their extremely narrow resonance linewidth. Theoretically, these dielectric resonators have shown a promise for ultra-small detection limits [1]; however, in practice, there are challenges in implementing these resonators mainly because they are sensitive to fabrication imperfections (especially to the surface roughness) [1, 5]. The resonance linewidth of a purely dielectric resonator is typically very small resulting in small spectral efficiency when a wideband source (e.g., a light emitting diode) is used. Thus, purely dielectric resonators are more suitable for applications in which a tunable laser source can be used. In addition, although an extremely small resonance linewidth results in better detection limits, it makes the device more sensitive to environmental changes such as thermal drift and drift of the source. Recently, there have been some efforts to stabilize dielectric resonators and make them less sensitive to temperature changes [36] by covering the resonator with a layer of polymer. However, this approach is not very compatible with the sensing application since covering of the structure with polymer reduces the interaction of the resonator mode with the target analyte. The proposed hybrid resonator in this paper has a wider resonance linewidth in comparison with a dielectric resonator (with the same material and radius) and therefore, has a larger spectral efficiency when used with a wideband source. It is also less sensitive to environmental changes such as temperature drifts. Besides the simplicity of the system and the spectral efficiency, another advantage of using a wideband source is that the output spectrum can be monitored in real-time when the sensor is integrated with a micro-spectrometer [16, 17], without any need for repeatedly scanning the spectrum. This makes the study of kinetic changes possible.

5 Conclusion

The hybrid resonator introduced in this paper is realized through coupling of the surface plasmon resonance mode (determined by metal-cladding material properties) and the whispering gallery resonance mode (determined by the geometry of the structure). The low-loss supermode of this structure has the high-sensitivity properties of the surface plasmon wave excited on the top and the narrow spectral linewidth characteristics of the dielectric (Si_3N_4) traveling-wave ring resonator. The sensitivity of the device is calculated to be 150 nm/RIU in the optimum operation range for reasonable device dimensions. The performance of this hybrid resonator sensor according to the values of FOM being around 76.9 compares well with other conventional guided wave SPR systems and is much larger than FOM values of LSPR sensors. The proposed sensor is very compact and can be used in a multiplexed scheme on a chip in an integrated platform. The quality factor of the hybrid resonator is mostly determined by the metal material loss and therefore, the device is tolerant to fabrication imperfections that introduce additional losses. Since the linewidth is not extremely narrow, no stringent requirements are needed in terms of source stability or thermal drifts. Due to the compact size, the high sensitivity, and the possibility of extension to multi-analyte detection, we believe that the hybrid resonator proposed here has the potential of enabling new applications in lab-on-a-chip sensing.

References

1. X. Fan, I.M. White, S.I. Shopva, H. Zhu, J.D. Suter, Y. Sun, Anal. Chem. Acta **620**, 8 (2008)
2. J. Homola, *Surface Plasmon Resonance Based Sensors*. Springer Series on Chemical Sensors and Biosensors, vol. 4 (Springer, Berlin, 2006)
3. A. Densmore, D.-X. Xu, P. Waldron, S. Janz, P. Cheben, J. Lapointe, A. Delage, B. Lamontagne, J.H. Schmid, E. Post, IEEE Photonics Technol. Lett. **18**, 2520 (2006)
4. R. Philip-Chandy, P.J. Scully, P. Eldridge, H.J. Kadim, M. Gerard Grapin, M.G. Jonca, M.G. D'Ambrosio, F. Colin, IEEE J. Sel. Top. Quantum Electron. **6**, 764 (2000)
5. K.D. Vos, I. Bartolozzi, E. Schacht, P. Bienstman, R. Baets, Opt. Express **15**, 7610 (2007)
6. A.M. Armani, R.P. Kulkarni, S.E. Fraser, R.C. Flagan, K.J. Vahala, Science **317**, 783 (2007)
7. E. Chow, A. Grot, L.W. Mirkarimi, M. Sigalas, G. Girolami, Opt. Lett. **29**, 1093 (2004)
8. B. Liedberg, C. Nylander, I. Lundstrom, Sens. Actuators **4**, 299 (1983)
9. F.B. Myers, L.P. Lee, Lab. Chip. **8**, 2015 (2008)
10. J. Dostalek, H. Vaisocherova, J. Homola, Sens. Actuators B **108**, 758 (2005)
11. S. Fang, H.J. Lee, A.W. Wark, R.M. Corn, J. Am. Chem. Soc. **128**, 1404 (2006)
12. R.D. Harris, J.S. Wilkinson, Sens. Actuators B: Chem. **29**, 261 (1995)
13. R. Slavik, J. Homola, J. Ctyroky, E. Brynda, Sens. Actuators B **74**, 106 (2001)
14. Z. Qi, I. Honma, H. Zhou, Appl. Phys. Lett. **90**, 181112 (2007)
15. M.W. Kim, Y.-H. Chen, J. Moore, Y.-K. Wu, L.J. Guo, P. Bhattacharya, P.C. Ku, J. Sel. Top. Quantum Electron. **15**, 1551 (2009)
16. B. Min, E. Ostby, V. Sorger, E. Ulin-Avila, L. Yang, X. Zhang, K.J. Vahala, Nature **457**, 455 (2009)
17. B. Momeni, E.S. Hosseini, M. Askari, M. Soltani, A. Adibi, Opt. Commun. **282**, 3168 (2009)
18. M. Chamanzar, B. Momeni, A. Adibi, Opt. Lett. **34**, 220 (2009)
19. A.G. Koutsioubas, N. Spliopoulos, D.L. Anastassopoulos, A.A. Vradis, G.D. Priftis, Mater. Sci. Eng. B **165**, 270 (2009)
20. A.G. Koutsioubas, N. Spliopoulos, D.L. Anastassopoulos, A.A. Vradis, G.D. Priftis, J. Appl. Phys. **103**, 094521 (2008)
21. F.S. Linger, C.R. Taitt, *Optical Biosensors: Today and Tomorrow* (Elsevier, Amsterdam, 2008)
22. P.B. Johnson, R.W. Christy, Phys. Rev. B **6**, 4370 (1972)
23. J.E. Spanier, I.P. Herman, Phys. Rev. B **61**, 10437 (2000)
24. M. Soltani, Ph.D. dissertation, Dept. Elect. Eng., Georgia Institute of Technology, Atlanta, GA (2009)
25. I.M. White, X. Fan, Opt. Express **16**, 1020 (2008)
26. A. Yariv, Electron. Lett. **36**, 321 (2000)
27. L.J. Sherry, R. Jin, C.A. Mirkin, G.C. Schatz, R.P. Van Duyne, Nano Lett. **6**, 2060 (2006)
28. K. Vahala, *Optical Microcavities* (World Scientific, Singapore, 2004)
29. M.K. Chin, S.T. Ho, J. Lightwave Technol. **16**, 1433 (1998)
30. W. Bogaerts, P. Dumon, D.V. Thourhout, D. Taillaert, P. Jaenen, J. Wouters, S. Beckx, R. Baets, J. Sel. Top. Quantum Electron. **12**, 1394 (2006)
31. E. Shah Hosseini, S. Yegnanarayanan, A.H. Atabaki, M. Soltani, A. Adibi, Opt. Express **18**, 14543 (2010)
32. T.M. Squires, R.J. Messinger, S.R. Manalis, Nature Biotechnol. **26**, 417 (2008)
33. E. Krioukov, D.J.W. Klunder, A. Driessen, J. Greve, C. Otto, Opt. Lett. **27**, 512 (2002)
34. A. Yalcın, K.C. Popat, J.C. Aldridge, T.A. Desai, J. Hryniewicz, N. Chbouki, B.E. Little, O. King, V. Van, S. Chu, D. Gill, M. Anthes-Washburn, M.S. Unlu, J. Sel. Top. Quantum Electron. **12**, 148 (2006)
35. F. Vollmer, S. Arnold, Nature Methods **5**, 1591 (2008)
36. J. Teng, P. Dumon, W. Bogaerts, H. Zhang, X. Jian, X. Han, M. Zhao, G. Morthier, R. Baets, Opt. Express **17**, 14627 (2009)